Journal of Environmental Chemical Engineering 13 (2025) 115048

Contents lists available at ScienceDirect

Journal of Environmental Chemical Engineering

journal homepage: www.elsevier.com/locate/jece

Construction of MnO_x with abundant surface hydroxyl groups for efficient ozone decomposition

Xiao Chen [a,*], Changcheng Zhou [b], Chonglai Chen [a], Chaoqun Bian [a], Ying Zhou [b], Hanfeng Lu [b,*]

[a] Department of Safety and Environmental Protection, Pharmaceutical College, Jinhua University of Vocational Technology, Jinhua 321017, China
[b] Innovation team of air pollution control, Institute of Catalytic Reaction Engineering, College of Chemical Engineering, Zhejiang University of Technology, Hangzhou 310014, China

ARTICLE INFO

Keywords:
MnO_x catalysts
Hydroxyl groups
Ozone decomposition
Water resistance
Mn valence states

ABSTRACT

Designing and constructing stable and high-performance catalysts for room-temperature ozone decomposition under humid conditions remains a significant challenge. Herein, we report manganese oxide (MnO_x) rich in surface hydroxyl groups (-OH), synthesized through a facile three-step process combining solid-state grinding, heat treatment, and hydrothermal activation using potassium permanganate and ascorbic acid as precursors. The as-prepared catalyst (MnO_x-A) demonstrated remarkable stability with 100 % ozone conversion maintained for 240 min under ≤ 50 % relative humidity (RH). Notably, it achieved 90 % ozone conversion after 240 min even under 90 % RH, surpassing its performance (79 % conversion) at 70 % RH. Through comprehensive characterization and density functional theory calculations, we revealed that the abundant surface -OH groups effectively mitigate the water-induced deactivation of MnO_x during room-temperature catalytic ozone decomposition under humid conditions. Furthermore, we established a correlation between the catalytic activity of -OH groups and the manganese valence state. These findings provide valuable insights for the rational design of highly efficient and stable catalysts for practical ozone elimination applications.

1. Introduction

Ozone (O_3), a powerful oxidizing agent, poses significant health risks to humans even at relatively low concentrations (>1 $\times 10^{-7}$ by volume). With growing attention to ground-level O_3 issues, there are increasing concerns about O_3 pollution in living, working and public spaces [1,2]. As O_3 plays a huge role in areas like food preservation, healthcare, and environmental remediation [3–5], effectively preventing O_3 pollution caused by residual O_3 from these processes is crucial for protecting human health. This requires the timely removal of remaining O_3 using efficient control technologies.

Among the many reported O_3 removal methods, catalytic decomposition can achieve rapid O_3 decomposition at room temperature without secondary pollution. It has attracted wide attention from researchers for its high research value and application potential [6–8]. The core of the catalytic method is the catalyst. In recent years, many efficient catalysts for ozone decomposition have been reported, among which manganese oxides (MnO_x) have been favored by researchers and studied extensively as the most promising ozone decomposition catalysts due to their advantages of low cost, abundant resources, environmental friendliness, and easy tunability [9–11]. Unfortunately, due to similar chemical structures, water vapor in the environment can compete with ozone for adsorption on the active sites (oxygen vacancies) of the catalyst, causing water-induced catalyst deactivation [12–27]. Therefore, maintaining the high efficiency and stability of MnO_x catalysts for catalytic ozone decomposition under humid conditions is a major challenge.

Studies have shown that doping MnO_x (e.g. with Ce, Co, Fe, W, Ni, Cu) can introduce abundant V_O to improve catalytic activity for O_3 decomposition under high humidity [28–33]. Similarly, ion-modification has also been widely studied. For example, Cao et al. [34] successfully introduced abundant V_O by using NH^{4+} to regulate the synthesis of ultrathin δ-MnO_2 nanosheets, imparting high stability for catalytic O_3 decomposition under high humidity. Zhu et al. [35] prepared α-MnO_2 nanowires with tunable K^+ concentrations, where increasing K^+ concentration enhanced the oxygen vacancy content, leading to higher catalytic O_3 decomposition performance under humid conditions. Hong et al. [36] significantly increased the number of V_O in OMS-2 catalysts by incorporating Na^+, positively impacting O_3 decomposition performance under humid conditions.

* Corresponding authors.
E-mail addresses: morningchenxiao@163.com (X. Chen), luhf@zjut.edu.cn (H. Lu).

https://doi.org/10.1016/j.jece.2024.115048
Received 20 August 2024; Received in revised form 23 October 2024; Accepted 5 December 2024
Available online 6 December 2024

In addition to these methods of increasing oxygen vacancy content, preventing water molecules from occupying vacancies has also been used to improve MnO_x catalytic activity for O_3 decomposition in humid environments. For example, Dai et al. [37] prepared a δ-MnO_2 supported on activated carbon (Mn/AC-A) that could stably catalyze O_3 decomposition under humid conditions, attributed to the functionalized AC suppressing water accumulation on the δ-MnO_2. Zhu et al. [27] encapsulated α-MnO_2 nanowires in a hydrophobic graphene shell to prevent V_O being occupied by water molecules, enhancing anti-moisture ability during catalytic O_3 decomposition. Liu et al. [38] found on c-disordered birnessite that, compared to the in-layer V_O, the out-of-layer V_O exhibited stronger adsorption of O_3 and weaker adsorption of H_2O, and the synthesized highly c-disordered birnessite with out-of-layer V_O exhibited high catalytic activity and stability for O_3 decomposition under humid conditions. Although these strategies can greatly improve the catalytic activity and stability of MnO_x for O_3 decomposition under humid conditions, limited by the intrinsic nature of oxygen vacancies, the competitive adsorption issue between environmental water vapor and ozone still exists. Therefore, regulating oxygen vacancies to maintain the high efficiency and stability of MnOx catalysts for catalytic ozone decomposition under humid conditions has fundamental deficiencies in terms of economy, convenience, and reliability. In recent years, with the proposal of the H-transfer redox mechanism of hydroxyl groups (-OH) as the active site for catalytic ozone decomposition [39–41], water vapor in the environment has also been considered beneficial for catalytic O3 decomposition. Wang et al. [42] constructed a metal organic framework (MIL-100 (Fe)) that exhibited excellent O_3 decomposition activity at relative humidity (RH) ≥ 40 % (100 % O_3 decomposition after 12 h reaction). Whereas under near-dry gas conditions (RH<5 %) the O_3 decomposition rate was only 10 %, indicating beneficial effects of water for decomposition. Sun et al. [43] synthesized a manganese-based metal organic framework ($[Mn_3(\mu_3\text{-}OH)_2(TTPE)(H_2O)_4]\cdot 2\,H_2O$, ZZU-281) from $Mn(NO_3)_2\cdot 6\,H_2O$ and H_4TTPE that could effectively eliminate O_3 over the entire humidity range from dry gas (≤5 % RH) to high humidity (90 % RH). Analysis showed this was attributed to stable coordinated water molecules and hydroxyl groups (-OH) activated by Mn^{2+} as active sites catalyzing the conversion of O_3 to oxygen. Although the presence of -OH on the surface of MnO_x with oxygen vacancies as the main active sites for catalytic ozone decomposition is detrimental [44], if rich -OH are constructed on the MnOx surface to replace oxygen vacancies as the main active sites for catalytic ozone decomposition, could this alleviate the water-induced deactivation issue of MnOx catalysts for room-temperature catalytic ozone decomposition (Fig. 1)?

In this work, we developed a novel MnO_x catalyst for room-temperature O_3 decomposition through a hydrothermal synthesis approach, utilizing the redox reaction between potassium permanganate and organic acids. Through a series of characterization tests and computational analyses, we found that the presence of abundant -OH enhance the catalytic performance of MnO_x for O_3 decomposition under humid conditions at room temperature. Furthermore, we investigated the factor affecting surface -OH in catalyzing O_3 decomposition. This work will enrich our understanding of MnO_x materials for catalytic O_3 decomposition from a new perspective and provide insights for the development of stable and efficient room-temperature O_3 decomposition catalysts applicable in practical environments.

2. Experimental

2.1. Catalyst preparation

All reagents are of analytical grade and used without any further purification. The MnO_x nanomaterials were synthesized via a solid-state grinding and hydrothermal activation method using potassium permanganate and organic acids as precursors. Specifically, $KMnO_4$ (6 mmol) and an organic acid (citric acid, ascorbic acid, or tartaric acid, 6 mmol) were thoroughly ground together for 2 min and then heat-treated at 100 °C for 30 min. After cooling to room temperature, deionized water (30 mL) was added, and the mixture was stirred until homogeneous. The resulting suspension was then hydrothermally activated at 100 °C under atmospheric pressure for 1 h. Subsequently, the precipitate was collected by centrifugation, washed several times with deionized water, and dried at 120 °C for 1 h to obtain the final product. The sample prepared using citric acid as the precursor was denoted as MnO_x-C, the one using ascorbic acid was labeled MnO_x-A, and the one using tartaric acid was named MnO_x-T. MnOx-A was treated at 150 °C for 1 h in air or N_2 atmosphere, denoted as Dehydrated (air) and Dehydrated (N_2), respectively. Dehydrated MnOx-A was hydrothermally treated at 100 °C under atmospheric pressure for 1 h. Subsequently, the precipitate collected by centrifugation was dried at 120 °C for 1 h, and the resulting product was denoted as Re-hydrothermal.

MnO_x monolithic catalyst was prepared through the following steps: 3 g MnO_x-A powder catalyst, 3 g silica sol (containing 30 % silica), and 24 g deionized water were mixed and ball-milled for 3 h. Then, cylindrical cordierite (Φ=1.5 cm, h=1 cm) was placed in the obtained slurry and ultrasonically impregnated for 1 h. The residual liquid in the channels was blown off with an air gun, and the samples were dried in a 70 °C oven for 12 h to obtain monolithic catalyst, designated as MnO_x/CH.

2.2. Catalyst characterization

X-ray diffraction (XRD) patterns were collected via an X-ray diffractometer (PANalytical X'Pert PRO, λ=0.1542 nm). X-ray photoelectron spectroscopy (XPS) was performed to identify the valence states and surface composition of the catalysts on a Kratos AXIS Ultra DLD spectrometer. Thermogravimetric (TG) analysis was conducted on a Netzsch STA 409PC. Infrared spectra were examined through Fourier transform infrared (FTIR) spectroscopy (Vertex 70, Bruker Optics, Germany). The hydroxyl group content was determined by potentiometric titration experiments conducted using a ZDJ-4B automatic potential titrator and more details are shown in the Supporting Material. Scanning

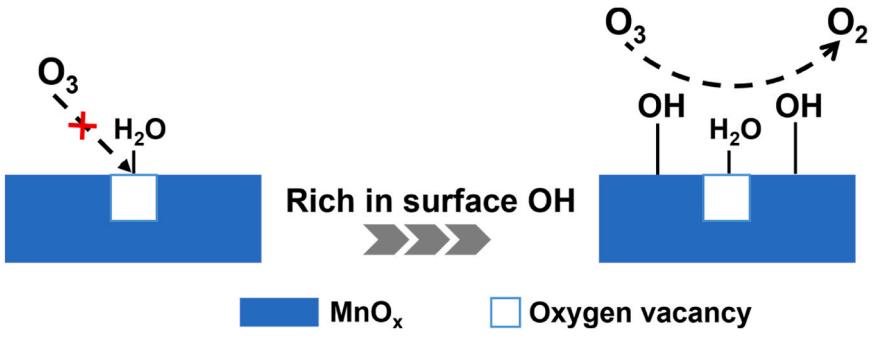

Fig. 1. Proposed strategy to alleviate water-induced deactivation of MnO_x catalysts for room-temperature O_3 decomposition.

electron microscopy (SEM) images were obtained on a Hitachi S-4700 (II) microscope operating at 15.0 kV. N_2 adsorption-desorption isotherms of the samples were carried out at 77 K on a Micromeritics ASAP2020 instrument. The specific surface area was determined by the Brunauer-Emmett-Teller (BET) method, and the pore size distribution was calculated by using the Barrett-Joyner-Halenda (BJH) formula from the desorption branch of the isotherms. H_2 temperature-programmed reduction (H_2-TPR) was measured on a FINE SORB-3010 E instrument equipped with a thermal conductivity detector (TCD). Electron paramagnetic resonance (EPR) spectra were recorded on a Bruker EMX plus 10/12 spectrometer (X-band, 9.84 GHz, 2 mW, 100 kHz modulation). Water contact angle measurement was carried out on a JY-82B Kruss DSA contact angle-measuring device. Density functional theory (DFT) calculations were performed for adsorption energy and reaction energy and more details are shown in the Supporting Material. In situ infrared test (in-situ DRIFTS) of ozone decomposition on the catalysts was operated with the scanning range of 4000–600 cm^{-1} by Fourier transform infrared spectroscopy (Vertex 70, Bruker Optics, Germany). The spectra were recorded for a series of time points with a total gas flow 50 % RH O_3/air rate of 50 $mL{\cdot}min^{-1}$.

2.3. Performance test

The catalytic activity of as-synthesized samples for O_3 decomposition was evaluated in a continuous fixed-bed reactor at 25 °C. Briefly, 100 mg sample was loaded in a quartz tube with an inner diameter of 6 mm and the total gas flow was 1 $L{\cdot}min^{-1}$. O_3 was generated by passing oxygen through an O_3 generator (COM-AD-01-OEM, Anseros Company, Germany) and was adequately mixed with dried clean air to maintain a 40 ppm concentration. The inlet and outlet O_3 concentration were monitored using an O_3 detector (Model 106-M, 2B Technologies Inc., USA). The relative humidity (RH) was controlled by adjusting the flow rate through the water bubbling bottle. The O_3 conversion was calculated as follows:

$$O_3 \text{ conversion } (\%) = (C_{in}\text{-}C_{out})/C_{in} \times 100\%$$

where C_{in} and C_{out} are inlet and outlet O_3 concentration, respectively.

Activity Regeneration Testing of MnOx/CH: Initially, the activity of fresh MnOx/CH was tested under a flow of air with a relative humidity of 70 % and an ozone concentration of 40 ppm for 2 h, referred to as Fresh. Following this, the sample underwent regeneration treatment (I) at 100 °C for 2 h, after which its activity was retested under the same conditions for 2 h, referred to as Cycle-1. Next, the sample was subjected to regeneration treatment (II) using water vapor at 100 °C for 2 h, and its activity was again tested under the same conditions for 2 h, referred to as Cycle-2. Subsequently, the sample underwent regeneration treatment (III) with ethanol-water vapor at 100 °C for 2 h, followed by activity test for 2 h under the same conditions, referred to as Cycle-3. After each regeneration treatment, prior to the activity test, the sample was placed in a desiccator and dried at room temperature for 12 h.

3. Results and discussion

3.1. Surface -OH and O_3 decomposition performance of as-prepared MnO_x

Fig. 2a schematically illustrates the synthesis of MnO_x catalysts via a combined approach of solid-state grinding, heat treatment, and ambient

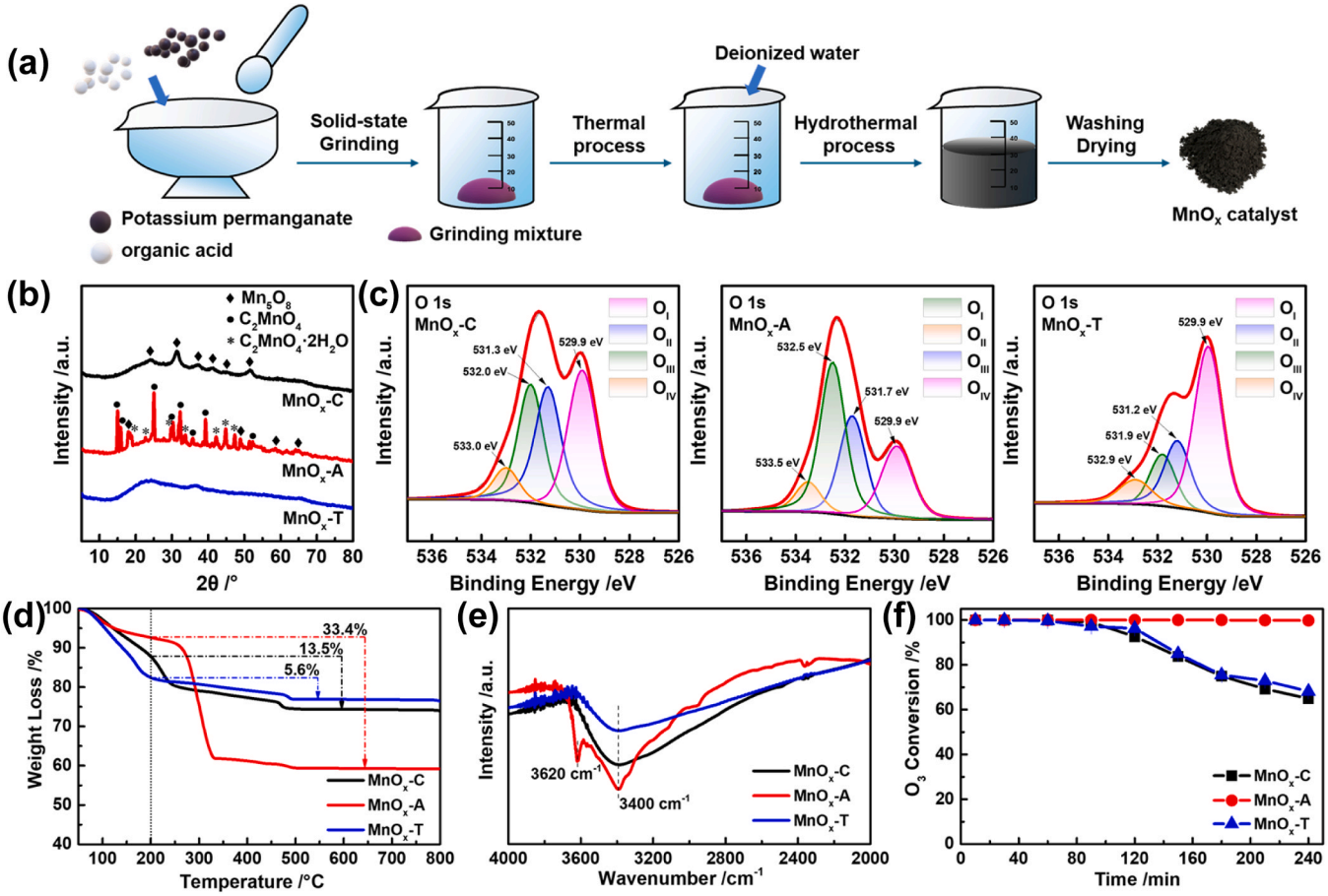

Fig. 2. (a) Schematic illustration of the synthesis procedure for MnO_x catalysts; (b) XRD patterns, (c) O 1 s XPS spectra, (d) thermogravimetric curves, (e) infrared spectra, (f) O_3 conversion of MnO_x-C, MnO_x-A, and MnO_x-T, reaction conditions: ~40 ppm O_3, RH= 50 %, catalyst usage: 100 mg, flow rate:1 $L{\cdot}min^{-1}$, 25 °C.

pressure hydrothermal activation using potassium permanganate and organic acids as precursors. The more information of the synthesis method is presented in the section of Experimental. XRD was used to identify the crystal structures of the prepared MnO_x catalysts and their patterns are shown in Fig. 1b. The diffraction peaks for the MnO_x-C sample at $2\theta = 24.1°$, 31.2°, 37.0°, 40.5°, 44.5°, 51.4°, 59.4°, and 66.2° could be assigned to Mn_5O_8 (PDF#39–1218). The MnO_x-T had similar diffraction peaks, but only three weak peaks at $\theta = 24.1°$, 37.0°, and 66.2° were observed, revealing its relatively poor crystallinity. For the MnO_x-A sample, the XRD pattern revealed the presence of MnC_2O_4 (PDF#32–0646) and $MnC_2O_4{\cdot}2\,H_2O$ (PDF#25–0544), which were insoluble products generated from the reaction of potassium permanganate and ascorbic acid. These byproducts were not removed in the washing process (the presence of yellow powder in the filter cake supports this, Fig. S1). Similarly, weak diffraction peaks related to Mn_5O_8 were also observed. The XRD result suggests that the product obtained through the hydrothermal reaction under atmospheric pressure conditions, utilizing the redox reaction between potassium permanganate and organic acids, is likely to be low-crystallinity Mn_5O_8. Generally, low crystallinity materials tend to have abundant defects and active sites on their surfaces [24,45,46], imparting them with better catalytic performance.

To elucidate the surface -OH content of the prepared samples, a series of characterizations were conducted. XPS experiments were conducted to study the chemical state of surface oxygen in all the samples. As shown in Fig. 2c, three peaks at 529.3–530.4 eV, 530.5–531.7 eV, and 531.8–532.6 eV and above 532.7 eV were attributed to O_I (lattice oxygen, O_{latt}), O_{II} (surface adsorbed oxygen, C═O, etc.), O_{III} (-OH), and O_{IV} (H_2O). [47–54], respectively. Notably, MnOx-A exhibits significantly higher binding energies compared to MnOx-C and MnOx-T, which may be attributed to its lower electron density. Table 1 lists the proportions of various oxygen species, showing that the prepared samples possessed abundant surface -OH, particularly MnOx-A. Furthermore, the samples were characterized by thermogravimetric analysis and infrared spectroscopy. Thermogravimetric analysis was conducted on the samples under nitrogen atmosphere, with results shown in Fig. 2c. The mass loss below 200 °C can be ascribed to desorption of adsorbed water, while mass loss above 200 °C can be assigned to desorption of -OH [55–57]. For MnO_x-C, MnO_x-A, and MnO_x-T, the measured mass losses below 200 °C mass were 12.2 %, 7.4 %, and 17.6 %, respectively, and the mass losses above 200 °C were 13.5 %, 33.4 %, and 5.6 %, respectively. Fig. S2 demonstrates that the decomposition of MnC2O4 occurs at 400 °C under a nitrogen atmosphere. The MnOx-A sample exhibits no significant weight loss above 400 °C, suggesting that despite the detection of MnC2O4 impurities by XRD in MnOx-A, their content is likely minimal. Fig. 2d presents the infrared spectra of the three samples. The 3400 cm^{-1} band is generally considered to relate to molecular water [58,59]. Notably, a sharp peak was observed at 3620 cm^{-1} for MnO_x-A, which could be attributed to the emergence of -OH linked to Mn [60–62]. The thermogravimetric and infrared results corroborated that MnOx-A exhibited the most abundant surface hydroxyl groups in comparison with MnOx-C and MnOx-T.

Based on Fig. 1, MnO_x-A was predicted to exhibit superior catalytic performance for O_3 decomposition under humid conditions compared to other samples. The catalytic performance of the as-synthesized MnO_x catalysts was evaluated at 25 °C under humid conditions (RH=50 %) with a weight hourly space velocity (WHSV) of 600000 $mL{\cdot}g^{-1}{\cdot}h^{-1}$ (Fig. 2f). As expected, MnO_x-A demonstrated excellent catalytic stability during the 240 min reaction period, while other samples showed notable activity deterioration over time. Fig. S3 shows that the MnC_2O_4 impurity in the MnO_x-A sample had negligible influence on its catalytic performance. Notably, although MnO_x-C possessed a higher concentration of surface -OH compared to MnO_x-T, they exhibited similar catalytic O_3 decomposition activities. Therefore, further verification is required to determine whether surface hydroxyl groups are indeed the primary active sites of as- synthesized MnO_x catalysts.

Table 1
O 1 s XPS results of MnO_x-C, MnO_x-A, and MnO_x-T.

Sample	O (%)			
	O_I	O_{II}	O_{III}	O_{IV}
MnO_x-C	34.3	31.0	27.5	7.2
MnO_x-A	23.1	26.9	41.8	8.2
MnO_x-T	53.9	22.4	14.3	9.4

3.2. Structure-activity relationship of as-prepared MnO_x

Analyzing the structure-activity relationship is crucial for accurately understanding the factors influencing catalytic performance. It is widely accepted that specific surface area and oxygen vacancies play important roles in O_3 decomposition. The morphologies of the prepared catalysts were characterized by SEM, as shown in Fig. 3a–c. The micrographs reveal distinct morphological features: MnO_x-C predominantly comprised wire-like particles, MnO_x-A exhibited nanorod arrays, while MnO_x-T consisted of rod-like and irregularly stacked particles. The pore structure and specific surface area of the samples were analyzed by nitrogen adsorption-desorption. As shown in Fig. 3d, all samples displayed type IV isotherms with characteristic hysteresis loops, indicative of mesoporous structures. The hysteresis loop profiles of MnO_x-C and MnO_x-A corresponded to H4 and H3 types, respectively, suggesting the presence of slit-like mesopores formed by nanoparticle aggregation, as corroborated by SEM observations (Fig. 3a and b). In contrast, MnO_x-T exhibited an H2-type hysteresis loop, signifying the existence of gap pores resulting from dense particle stacking (Fig. 3c). Pore size distribution analysis revealed a predominant range of 4–10 nm for all samples, with average pore size (Table 2) in the order of MnO_x-A> MnO_x-T > MnO_x-C, aligning with the SEM observations. Furthermore, we determined the specific surface areas (S_{BET}) of the samples using the Brunauer-Emmett-Teller method (Table 2). All samples possessed relatively large specific surface areas, especially MnO_x-A with a specific surface area up to 271 $m^2{\cdot}g^{-1}$. Typically, the larger specific surface area of catalyst, the more readily accessible the surface active sites are to O_3 molecules. This could explain why MnO_x-C and MnO_x-T exhibited similar catalytic O_3 decomposition activities.

The reducibility of the as-prepared samples was evaluated by H_2-TPR experiments. The reduction process of MnO_x typically follows the sequence $MnO_2 \rightarrow Mn_2O_3 \rightarrow Mn_3O_4 \rightarrow MnO$ [63–65]. The dark green color exhibited by all three samples after reduction indicates that they were reduced to MnO. The H_2-TPR profiles (Fig. 3e) reveal distinct reduction patterns for each sample. MnO_x-C sample exhibited reduction peaks at 250 °C and 418 °C. MnO_x-A sample (excluding the influence of C_2MnO_4) showed the main reduction peak at 270 °C with a small peak at 345 °C. MnO_x-T sample displayed reduction peaks at 260 °C and 427 °C. These results suggest that the MnO_x-A sample can be more easily reduced to MnO, indicating stronger oxygen activity. Consequently, compared to MnOx-C and MnOx-T, MnOx-A likely possesses a higher concentration of surface defects. Additionally, the order of hydrogen consumption amount was calculated as MnO_x-A (1.26 $mmol{\cdot}g^{-1}$) < MnO_x-C (1.51 $mmol{\cdot}g^{-1}$) < MnO_x-T (5.24 $mmol{\cdot}g^{-1}$), indicating that MnO_x-A has the lowest average manganese valence state.

To further determine the average manganese valence state in the samples, the Mn 3 s XPS spectra of the samples were analyzed (Fig. 3f) since Mn elements with different valence states have different splitting energies for the Mn 3 s peak. The average oxidation state (AOS) of the surface Mn atoms was calculated using the following relationship [66–68]:

$$AOS = 8.956 - 1.126 \times \Delta E$$

where ΔE is the Mn 3 s multiplet splitting energy. The results showed that the order of average manganese oxidation states in the synthesized

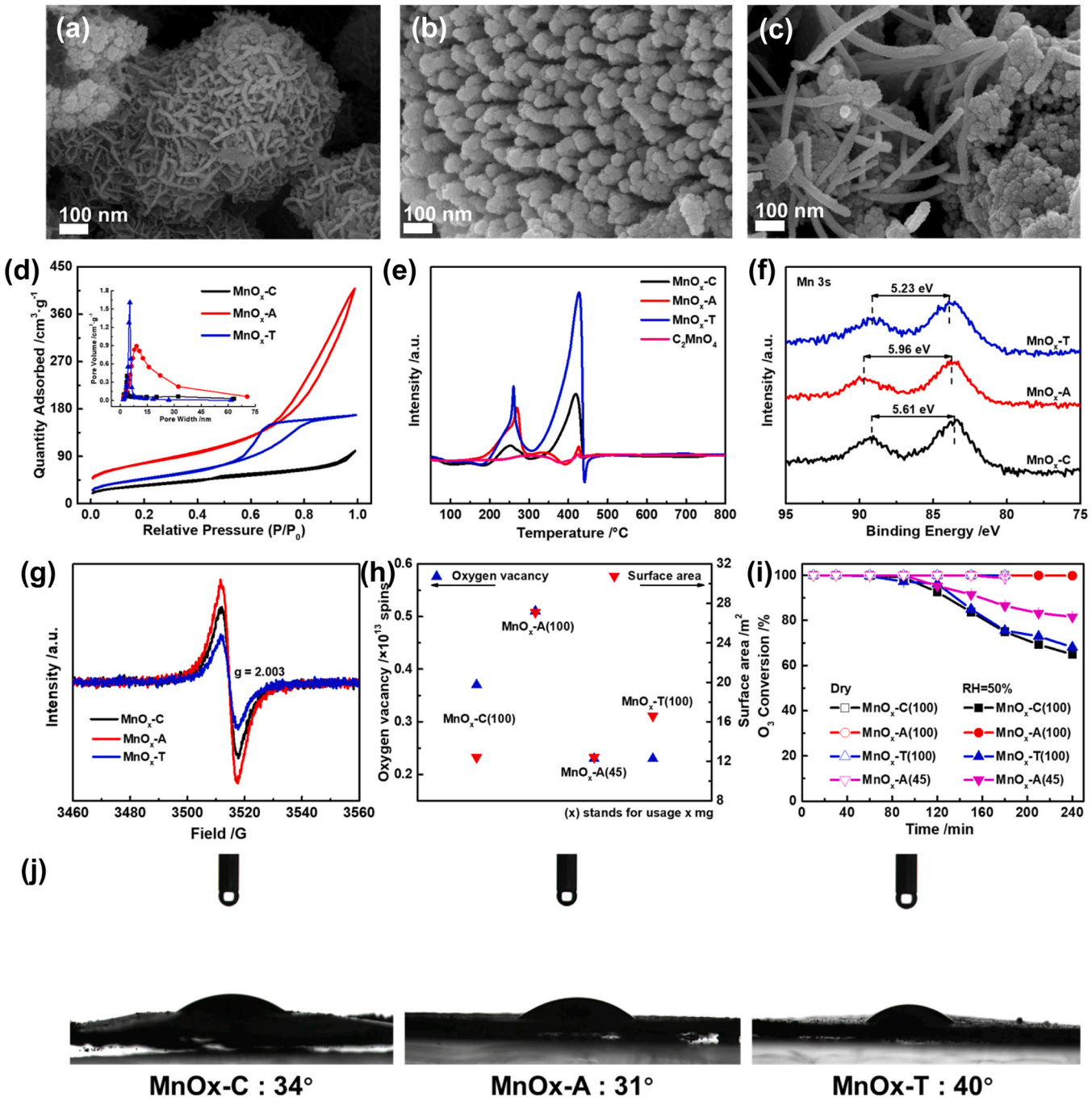

Fig. 3. SEM images of (a) MnO_x-C, (b) MnO_x-A, and (c) MnO_x-T; (d) N_2 adsorption-desorption isotherms and pore size distribution of MnO_x-C, MnO_x-A, and MnO_x-T; (e) H_2-TPR profiles of MnO_x-C, MnO_x-A, MnO_x-T and C_2MnO_4; (f) Mn 3 s XPS spectra and (g) EPR profile of MnO_x-C, MnO_x-A, and MnO_x-T; (h) Schematic representation of the oxygen vacancy and surface area, and (i) O_3 conversion of MnO_x-C(x), MnO_x-A(x), and MnO_x-T(x), (x) stands for usage x mg, reaction conditions: ~40 ppm O_3, RH= 50 %, flow rate:1 L·min^{-1}, 25 °C; (j) Water contact angle measurements of MnO_x-C, MnO_x-A, and MnO_x-T.

samples was MnO_x-A (2.2) < MnO_x-C (2.6) < MnO_x-T (3.0), consistent with the H_2-TPR results. EPR characterization was employed to quantify the V_O present in the three samples, as depicted in Fig. 3g and Table 2. In line with XRD and H_2-TPR analysis results, the as-synthesized samples exhibited a high concentration of defects (V_O), with MnO_x-A possessing the highest concentration of V_O.

Based on the aforementioned characterizations, the surface area and oxygen vacancy concentration for a given mass of each sample were calculated (Table 2) and presented them graphically in Fig. 3h for a more intuitive comparison. As illustrated, when the sample amounts were consistent (100 mg), MnO_x-A (100) exhibited the highest surface area and oxygen vacancy concentration, thus displaying the optimal catalytic O_3 decomposition performance. However, was its superior activity solely attributed to higher surface area and oxygen vacancy concentration? To address this, we adjusted the sample amounts to 100 mg MnO_x-C, 45 mg MnO_x-A, and 100 mg MnO_x-T, ensuring comparable surface areas and oxygen vacancy concentrations (Fig. 3h and Table 2). Subsequently, catalytic O_3 decomposition activity tests were conducted under identical conditions, with the results depicted in Fig. 3i. Interestingly, despite the surface area and oxygen vacancy concentration analysis suggesting that MnO_x-A(45) should exhibit lower catalytic O_3 decomposition activity compared to MnO_x-C(100) and

Table 2
Pore size, S_{BET} and V_O results of MnO_x-C, MnO_x-A, and MnO_x-T.

Sample	Pore size (nm)	S_{BET} ($m^2 \cdot g^{-1}$)	V_O (10^{13} spins$\cdot g^{-1}$)	Usage (mg)	Oxygen vacancy (10^{13} spins)	Surface area (m^2)
MnO_x-C	4	124	3.7	100	0.37	12.4
MnO_x-A	8	271	5.1	100 45	0.51 0.23	27.1 12.4
MnO_x-T	6	166	2.3	100	0.23	16.6

MnO_x-T(100), the experimental results were strikingly contradictory. Under humid conditions (RH=50 %), after 240 min of reaction, the O_3 conversion rate on MnO_x-A(45) was approximately 23 % higher than that on MnO_x-C(100) and MnO_x-T(100). Combined with the data obtained under dry conditions, this suggests that MnO_x-A demonstrates enhanced resistance to water-induced deactivation during the room-temperature catalytic O_3 decomposition. This behavior cannot be solely attributed to an increased surface area or higher oxygen vacancy concentration.

The difference in the resistance to water-induced deactivation among the samples may be attributed to the hydrophilicity or hydrophobicity of their surfaces. To gain insights into the surface wettability of the prepared samples, water contact angle measurements were performed. As shown in Fig. 3j, the water contact angles for MnO_x-C, MnO_x-A, and MnO_x-T were 34°, 31°, and 40°, respectively, indicating that the surface wettability of the three samples did not differ significantly, with MnO_x-A even exhibiting a higher affinity for water molecules. However, the activity tests (Fig. 4b) revealed that MnO_x-A possessed superior resistance to water-induced deactivation among the three samples. This phenomenon indicates MnO_x-A's superior resistance to water-induced deactivation during the room-temperature catalytic O_3 decomposition process is not attributable to a more hydrophobic surface. By analyzing the structure-activity relationship and excluding factors such as oxygen vacancies, surface area, and hydrophilicity/hydrophobicity, the result that MnO_x-A exhibits higher catalytic activity for room-temperature O_3 decomposition under humid conditions (Fig. 4i) further strengthens our hypothesis (Fig. 1): the surface -OH of MnOx could serve as primary active sites for the catalytic O_3 decomposition.

3.3. *Effect of surface -OH on O_3 decomposition performance*

To verify the role of surface -OH in catalytic O_3 decomposition, we investigated the effect of heat treatment on the surface hydroxyl content

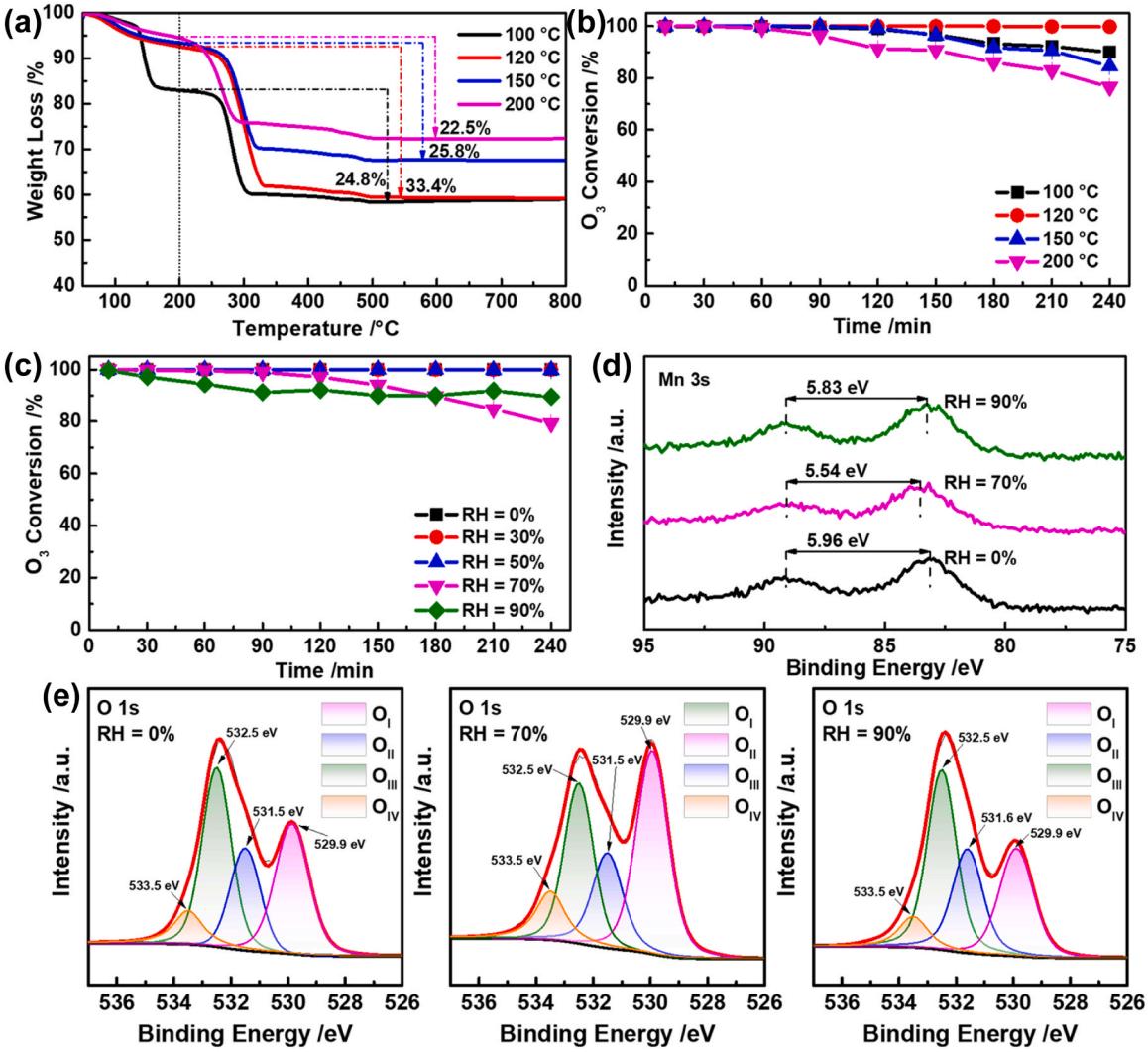

Fig. 4. (a) Thermogravimetric curves and (b) O_3 conversion of the hydrothermal products of potassium permanganate and ascorbic acid dried at 100 °C, 120 °C, 150 °C and 200 °C, reaction conditions: ~40 ppm O_3, RH= 50 %, catalyst usage: 100 mg, flow rate:1 L·min^{-1}, 25 °C; (c) O_3 conversion of MnO_x-A under different relative humidity; (d) Mn 3 s and (e) O 1 s XPS spectra of MnO_x-A after reacting for 240 min under 0 %, 70 %, and 90 % RH conditions.

of the samples. The hydrothermal products of potassium permanganate and ascorbic acid were dried at different temperatures (100 °C, 120 °C, 150 °C, 200 °C) for 1 h before evaluating their catalytic O_3 decomposition performance. Fig. 4a presents the TGA curves of the obtained samples. Generally, the surface -OH content (the mass loss above 200 °C) decreased with increasing drying temperature. The sample dried at 120 °C (MnO_x-A) exhibited the highest surface hydroxyl content, followed by those dried at 150 °C and 100 °C, while the sample dried at 200 °C showed the lowest -OH content. Notably, the sample dried at 100 °C did not exhibit the highest surface hydroxyl content, possibly due to insufficient drying, leading to the surface of the samples primarily containing adsorbed water. Fig. 4b shows the catalytic O_3 decomposition performance of these samples under 50 % relative humidity. Remarkably, the catalytic performance of the samples for O_3 decomposition correlated positively with their surface hydroxyl content. This result indicates that surface -OH can improve the performance of MnO_x catalysts for O_3 decomposition under humid conditions, and the catalytic performance can be optimized by controlling the content of surface -OH.

Further investigation into the catalytic performances of MnO_x-A for O_3 decomposition under different relative humidity as shown in Fig. 4c. Under 0 % (dry), 30 %, and 50 % RH conditions, the sample maintained 100 % removal of O_3 after 240 min of continuous running. However, a decline in activity was observed as the RH increased to 70 % and 90 %. Specifically, under the 70 % RH condition, the O_3 conversion dropped to 79 % after 240 min; under the 90 % RH condition, the O_3 conversion dropped to 90 % after 240 min. The higher O_3 decomposition activity of MnO_x-A under 90 % RH compared to 70 % RH indicates that the activity decline of MnO_x-A under humid conditions is not caused by the competitive adsorption of water and O_3. This indirectly suggests that abundant surface -OH can alleviate the water-induced deactivation issue of MnO_x catalysts for room-temperature O_3 decomposition.

To investigate the potential causes of the observed decline in material activity, MnO_x-A samples after reacting for 240 min under 0 %, 70 %, and 90 % RH conditions were characterized by XPS. Fig. 4d shows the Mn 3 s spectra of the samples, from which the average oxidation state of manganese to be 2.2 (0 %RH), 2.7 (70 %RH) and 2.4 (90 %RH), respectively. Fig. 4e shows the O 1 s spectra of the samples, and by peak-fitting, the proportions of various oxygen species were obtained (Table 3). It can be observed that with increasing relative humidity, the content of O_{III} on the sample surface after reaction first decreased and then increased, indicating that the water molecules adsorbed on the surface during the reaction were not stable. Under the 70 % RH condition, the majority of these molecules likely formed O_{latt}, with a small portion present as -OH. Conversely, under the 90 % RH condition, the predominant form appeared to be -OH, with a small portion forming O_{latt}. This could be the reason for the change in the average manganese valence state in the samples. Based on this characterization data activity analysis, the role of -OH in catalytic O_3 decomposition may be related to the manganese valence state: -OH connected to lower-valent manganese has superior catalytic performance to -OH connected to higher-valent manganese.

To corroborate our hypothesis, we devised an experiment involving MnO_x-A samples subjected to dehydration and re-hydrothermal treatments during different atmospheres. The catalytic performance of these samples in O_3 decomposition was then evaluated (Fig. 5a). Compared to the fresh MnO_x-A, the sample dehydrated under nitrogen atmosphere showed relatively good recovery of activity after re-hydrothermal, whereas the sample dehydrated under air atmosphere showed negligible recovery. This disparity can be attributed to the oxidizing effect of O_2 in air during dehydration, which likely increased the manganese oxidation state. Conversely, the nitrogen atmosphere served as an inert protective gas, preserving the initial manganese oxidation state. Consequently, when -OH were reintroduced through re-hydrothermal treatment, a significant difference in activity was observed between the two samples. This result essentially confirms that the activity of -OH in catalytic O_3 decomposition is indeed related to the manganese valence state.

Furthermore, we conducted deactivated catalyst regeneration experiments. To better align with practical applications and facilitate regeneration operations, we prepared MnO_x/CH monolithic catalysts for activity and regeneration testing. More information of the preparation and testing method is presented in the section of Experimental. Fig. 5b shows the performance of the fresh and differently regenerated MnO_x/CH for O_3 decomposition. Taking the activity of the fresh catalyst as the baseline, it can be found that Cycle-1 regained a small amount of activity, Cycle-2 showed a partial recovery of activity, and Cycle-3 exhibited a significant recovery. These changes can be explained as follows: First, the fresh catalyst has a certain amount of surface V_O and -OH, and the average manganese valence state is relatively low. During the catalytic O_3 decomposition process under 70 % RH, some V_O were occupied by water molecules or peroxides, and the manganese valence state increased, leading to decreased activity. After treatment I, the occupied V_O were partially released, but the average manganese valence state could not be reduced, so the activity was only slightly recovered. After treatment II, the hot steam would also release some V_O (not as effective as treatment I) and introduce a certain amount of -OH. This is because, as reported in the literature [69–71], due to the strong electric field (10^7 V/cm) at the air-water interface and the contact charging at the water-solid interface, -OH can spontaneously form at the micromolar level by condensing water vapor to form microdroplets on the solid surface. but the average manganese valence state remained largely unchanged, so the activity was also partially recovered. After treatment III, the hot steam released some V_O and introduced a certain amount of -OH, and the reducing nature of the alcohol vapor helped reduce the average manganese valence state [72,73]. With these favorable factors combined, the activity was significantly recovered. This result is consistent with the analysis of the influence of surface -OH on the performance of MnO_x catalysts for O_3 decomposition and also provides insights for designing and constructing efficient and stable MnO_x structures for room-temperature O_3 decomposition catalysis: rich surface -OH, low average manganese valence state, and the ability to maintain a stable manganese valence state during the catalytic process.

Table 3
O 1 s XPS results of MnO_x-A after reacting for 240 min under 0 %, 70 %, and 90 % RH conditions.

Sample	reaction condition (RH, %)	O (%)			
		O_I	O_{II}	O_{III}	O_{IV}
MnO_x-A	0	32.2	21.2	37.5	9.1
	70	41.1	19.1	28.8	11.0
	90	27.2	24.7	40.2	7.9

3.4. Density functional theory calculations

The aforementioned characterization and experimental results indicate that abundant surface -OH can alleviate the water-induced deactivation issue of MnO_x catalysts for room-temperature O_3 decomposition, and its activity expression is related to hydroxyl content and manganese valence state. Furthermore, density functional theory (DFT) calculations were conducted to investigate the influence of surface -OH on the catalytic performance of MnO_x for O_3 decomposition. First, the adsorption energies of O_3 and H_2O on different active sites (V_O and -OH) were compared by DFT calculations. Fig. 6a illustrates the structural model of Mn_5O_8 constructed with both V_O and -OH sites. The calculation results are shown in Fig. 6b. More negative adsorption energy indicates stronger adsorption. The adsorption energies of O_3 and water molecules on the V_O site were −0.329 eV and −0.559 eV, respectively, indicating that H_2O is more easily adsorbed on V_O, leading to worse catalytic O_3 decomposition performance. In contrast, the adsorption energies of O_3 and water molecules on the -OH site were −0.617 eV and −0.169 eV, respectively, indicating that O_3 is more easily adsorbed on -OH, and the

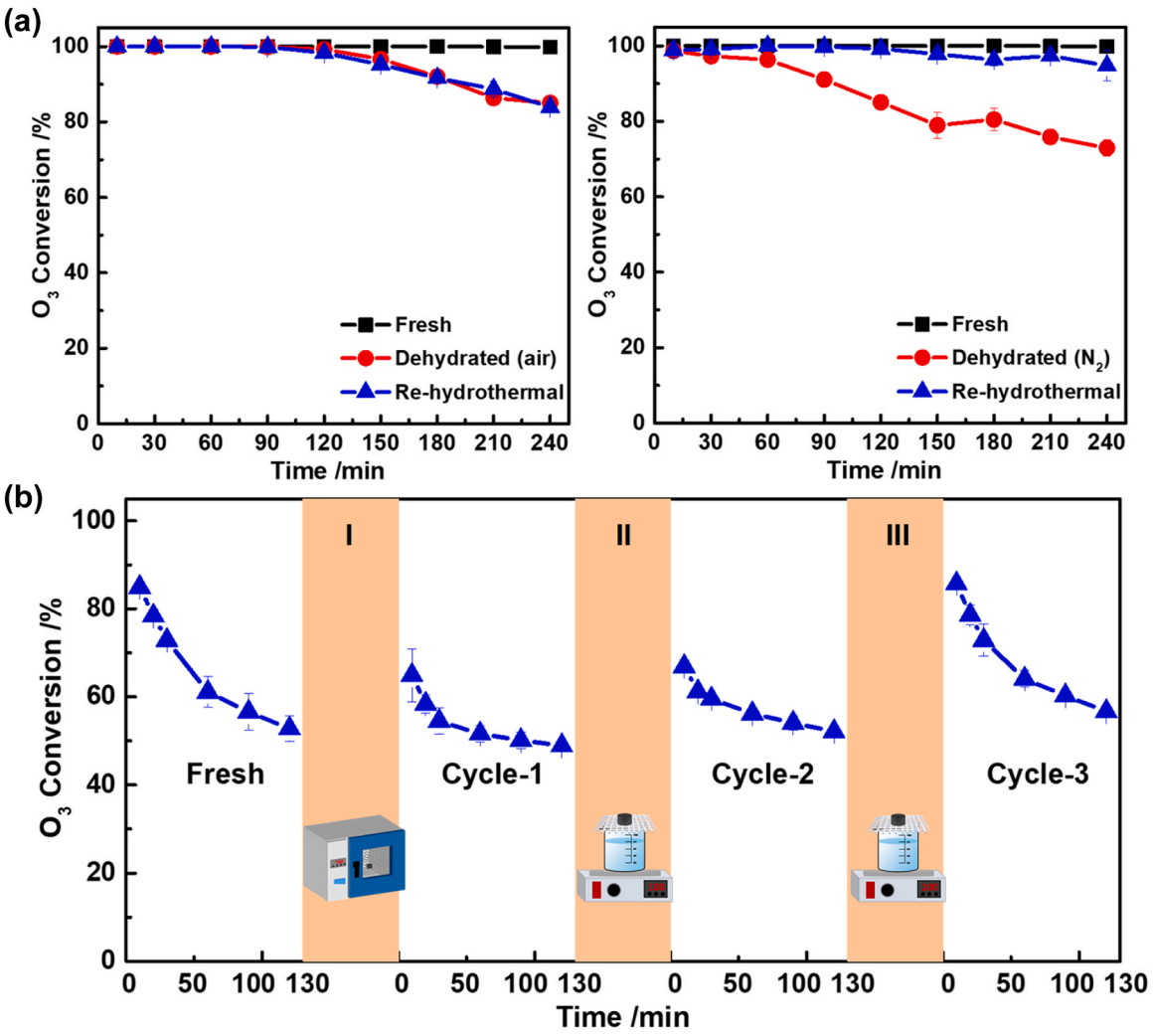

Fig. 5. (a) O_3 conversion of Fresh, dehydrated and re-hydrothermal MnO_x-A, reaction conditions: ~40 ppm O_3, RH= 50 %, catalyst usage: 100 mg, flow rate:1-L·min^{-1}, 25 °C; (b) O_3 conversion of fresh and regenerated MnO_x/CH, reaction conditions: ~40 ppm O_3, RH= 70 %, flow rate:1 L·min^{-1}, 25 °C.

presence of water molecules does not affect the adsorption of O_3 on -OH. This implies that abundant surface -OH are beneficial for the catalytic decomposition of O_3 by MnO_x in humid environments, consistent with the experimental results.

To further elucidate the catalytic decomposition mechanism of O_3 on the material surface, in situ DRIFT studies of O_3 decomposition on the MnO_x-A sample were conducted, as shown in Fig. 6c. The peaks at 670–823 cm^{-1} and 875–1103 cm^{-1} are attributed to the ozonide O_3^- species and physically adsorbed O_3 molecules, respectively. The peaks around 3000–3700 cm^{-1} are associated with the bending vibration of H_2O [40]. The results indicate that as the reaction progresses, the amount of adsorbed water on the MnO_x-A surface increases, but this does not significantly affect the adsorption and activation of ozone. This suggests that there is no competitive adsorption between ozone and water molecules on MnO_x-A, implying that oxygen vacancies are not the primary active sites. The findings corroborate that the catalytic ozone decomposition mechanism of the prepared MnO_x-A follows the H-transfer redox mechanism, with hydroxyl groups serving as the active sites.

Building upon above analysis and drawing from the literature [40, 43,74], the O_3 decomposition on -OH active sites follows the steps below (Fig. 6d): O_3 is adsorbed on -OH to form the OOOH intermediate (I, II) with the H in -OH; Two adjacent OOOH intermediates rearrange and release an oxygen molecule to form the HOOOOH intermediate (III); The HOOOOH intermediate rapidly dissociates to produce the OOH intermediate and an oxygen molecule (IV), and after releasing the oxygen molecule to expose a -OH active site (V); The OOH intermediate further generates an oxygen molecule and regenerates the -OH active site (VI) to return to its initial state (IS), where the transition from state V to state VI is the rate-determining step for the whole reaction. The reaction energies of the surface -OH catalyzing the O_3 decomposition process on the constructed Mn_5O_8 structural models were calculated by density functional theory. Fig. 6d shows the calculated reaction energy profiles of -OH connected to different valence Mn catalyzing O_3 decomposition. It can be seen that the -OH active sites on lower-valence Mn are easier to adsorb O_3 to form intermediates and thus promote O_3 decomposition compared to those on higher-valence Mn. Notably, the reaction barrier of the rate-determining step decreased by 0.25 eV, showing that -OH connected to lower-valence Mn exhibits enhanced catalytic activity for O_3 decomposition. This indicates that the activity of surface -OH on MnO_x in catalytic O_3 decomposition is related to the manganese valence state, which is consistent with the experimental results and provides theoretical support for the relevant analysis discussions.

4. Conclusions

In this work, MnO_x catalysts with abundant surface -OH were synthesized via a combined approach of solid-state grinding, heat treatment, and ambient pressure hydrothermal activation using potassium

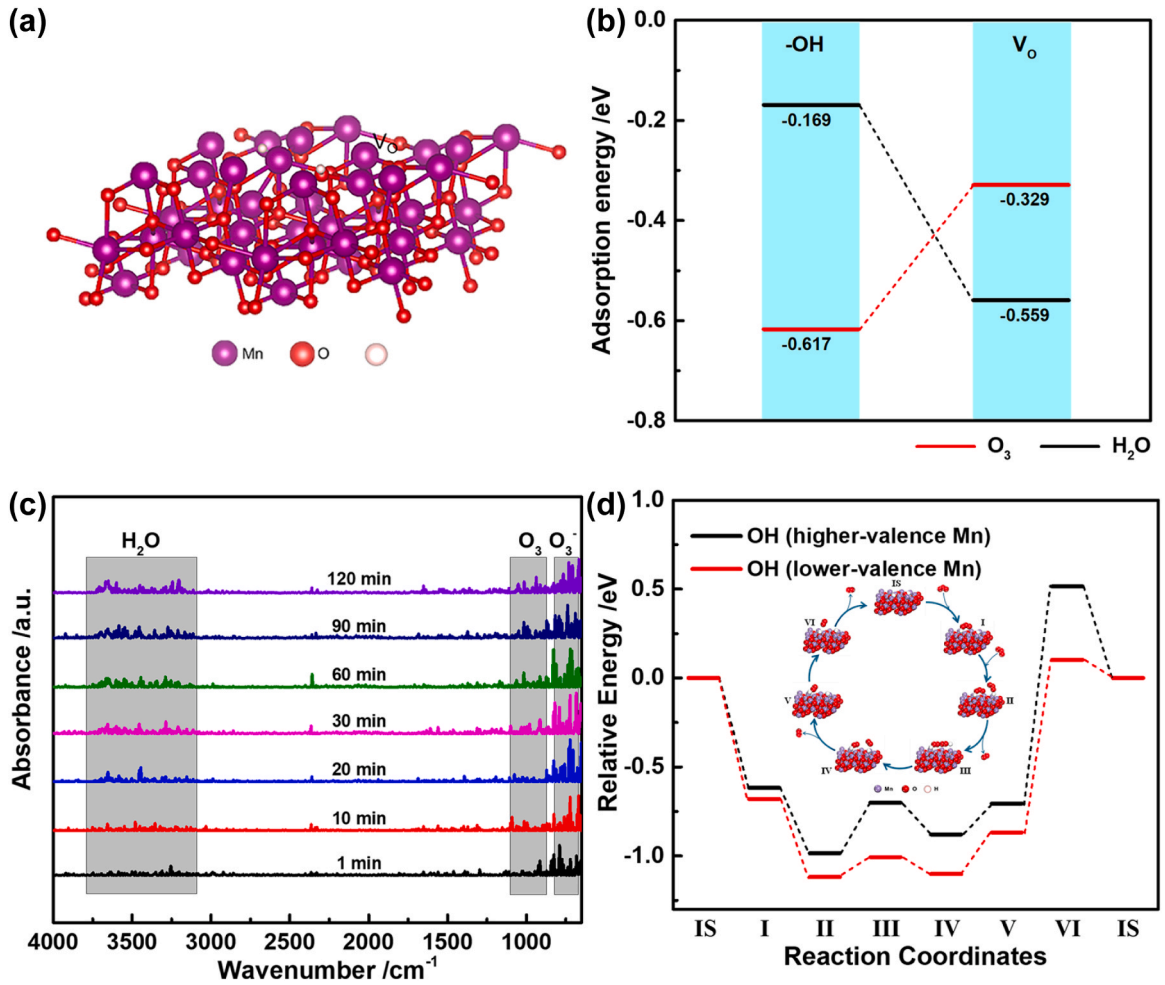

Fig. 6. (a) Structural model of Mn_5O_8 with V_O and -OH sites; (b) Adsorption energies of O_3 and H_2O on V_O and -OH; (c) In-situ DRIFT of MnOx-A under the flow of 50 % RH O_3/air; (d) Schematic diagram of O3 decomposition pathway on -OH and relative energy profiles for O_3 decomposition on -OH connected different valence Mn.

permanganate and organic acids as precursors. Comprehensive characterization techniques coupled with DFT calculations revealed that the abundant surface -OH can alleviate the water-induced deactivation issue of MnO_x catalysts for O_3 decomposition under humid environments, and the catalytic activity of -OH for O_3 decomposition was found to be related to the manganese valence state: -OH associated with low-valent Mn exhibit higher catalytic activity compared to those connected to high-valent Mn. Our findings not only prove that constructing surface -OH is an effective approach to improve the water-induced deactivation issue of MnO_x for room-temperature O_3 decomposition but also provide new insights into the design of efficient and stable manganese oxide catalysts for O_3 decomposition at room temperature.

CRediT authorship contribution statement

Ying Zhou: Supervision, Resources. **Hanfeng Lu:** Writing – review & editing, Resources, Project administration, Methodology, Funding acquisition, Conceptualization. **Chonglai Chen:** Validation, Formal analysis. **Chaoqun Bian:** Validation, Formal analysis. **Xiao Chen:** Writing – original draft, Methodology, Investigation, Funding acquisition, Formal analysis, Data curation, Conceptualization. **Changcheng Zhou:** Investigation, Formal analysis, Data curation.

Declaration of Competing Interest

The authors declare that they have no known competing financial interests or personal relationships that could have appeared to influence the work reported in this paper.

Acknowledgements

This work was supported by the National Key Research and Development Program of China (2022YFC3702003), Zhejiang Provincial Key Research and Development Program (2023C03127, 2024C03114), Zhejiang Provincial Fundamental and Public Welfare Technology Program (LTGS24E080008), General Research Projects of Zhejiang Provincial Education Department (Y202455693), and Jinhua Science and Technology Bureau (2022–4–006).

Appendix A. Supporting information

Supplementary data associated with this article can be found in the online version at doi:10.1016/j.jece.2024.115048.

Data availability

Data will be made available on request.

References

[1] Z.H. Jian, J. Cai, R.J. Chen, Y. Niu, H.D. Kan, A bibliometric analysis of research on the health impacts of ozone air pollution, Environ. Sci. Pollut. Res. 31 (2024) 16177–16187, https://doi.org/10.1007/s11356-024-32233-0.

[2] J.F. Zhang, Y.J. Wei, Z.F. Fang, Ozone pollution: a major health hazard worldwide, Front. Immunol. 10 (2019) 2518, https://doi.org/10.3389/fimmu.2019.02518.

[3] Y.J. Wang, Y.X. Li, S.H. Yang, Z.X. Wu, Y.X. Shen, Gaseous ozone treatment prolongs the shelf-life of fresh-cut kiwifruit by maintaining its ascorbic acid content, Lwt Food Sci. Technol. 172 (2022) 114196, https://doi.org/10.1016/j.lwt.2022.114196.

[4] E. Ogut, K. Armagan, Evaluation of the potential impact of medical ozone therapy on Covid-19: a review study, Ozone-Sci. Eng. 45 (2023) 213–231, https://doi.org/10.1080/01919512.2022.2065242.

[5] E.I. Epelle, A. Macfarlane, M. Cusack, A. Burns, J.A. Okolie, W. Mackay, M. Rateb, M. Yaseen, Ozone application in different industries: a review of recent developments, Chem. Eng. J. 454 (2023) 140188, https://doi.org/10.1016/j.cej.2022.140188.

[6] X. Chen, C.C. Zhou, Q.L. Ke, Y. Zhou, X.M. Zeng, Z.N. Jin, H.Y. Liu, H.F. Lu, Ethanol-thermal synthesis of colloidal-CeFeMn mixed-oxide as efficient catalytic material for atmospheric ozone decomposition, Colloid Surf. A 676 (2023) 132238, https://doi.org/10.1016/j.colsurfa.2023.132238.

[7] J.M. Ma, R.R. Cao, Y.L. Dang, J.L. Wang, A recent progress of room-temperature airborne ozone decomposition catalysts, Chin. Chem. Lett. 32 (2021) 2985–2993, https://doi.org/10.1016/j.cclet.2021.03.031.

[8] M. Namdari, C.S. Lee, F. Haghighat, Active ozone removal technologies for a safe indoor environment: a comprehensive review, Build. Environ. 187 (2021) 107370, https://doi.org/10.1016/j.buildenv.2020.107370.

[9] L.M. Ye, W.J. Dai, P. Lu, J.H. Huang, X.H. Yan, C.C. Sun, K. He, M.Y. Zhang, H. B. Huang, One-step synthesis of sludge-derived MnO_x catalysts for highly efficient removal of gaseous ozone from industrial flue gas, Appl. Catal. B 345 (2024) 123696, https://doi.org/10.1016/j.apcatb.2024.123696.

[10] H. Zhao, A.J. Wang, Q.Y. Zhang, C. Han, Highly efficient removal of ozone by amorphous manganese oxides synthesized with a simple hydrothermal method, J. Environ. Sci. 134 (2023) 96–107, https://doi.org/10.1016/j.jes.2022.10.019.

[11] L.X. Li, R.R. Cao, P.Y. Zhang, Catalytic decomposition of gaseous ozone at room temperature, Prog. Chem. 33 (2021) 1188–1200, https://doi.org/10.7536/PC200716.

[12] B. Dhandapani, S.T. Oyama, Gas phase ozone decomposition catalysts, Appl. Catal. B 11 (1997) 129–166, https://doi.org/10.1016/S0926-3373(96)00044-6.

[13] W. Li, G.V. Gibbs, S.T. Oyama, Mechanism of ozone decomposition on a manganese oxide catalyst. 1. In situ Raman spectroscopy and ab initio molecular orbital calculations, J. Am. Chem. Soc. 120 (1998) 9041–9046, https://doi.org/10.1021/ja981441+.

[14] W. Li, S.T. Oyama, Mechanism of ozone decomposition on a manganese oxide catalyst. 2. Steady-state and transient kinetic studies, J. Am. Chem. Soc. 120 (1998) 9047–9052, https://doi.org/10.1021/ja9814422.

[15] J.B. Jia, P.Y. Zhang, L. Chen, Catalytic decomposition of gaseous ozone over manganese dioxides with different crystal structures, Appl. Catal. B 189 (2016) 210–218, https://doi.org/10.1016/j.apcatb.2016.02.055.

[16] J.B. Jia, P.Y. Zhang, L. Chen, The effect of morphology of α-MnO_2 on catalytic decomposition of gaseous ozone, Catal. Sci. Technol. 6 (2016) 5841–5847, https://doi.org/10.1039/C6CY00301J.

[17] Z.H. Xu, W.H. Yang, W.Z. Si, J.J. Chen, Y. Peng, J.H. Li, A novel γ-like MnO_2 catalyst for ozone decomposition in high humidity conditions, J. Hazard. Mater. 420 (2021) 126641, https://doi.org/10.1016/j.jhazmat.2021.126641.

[18] C.T. Fang, C.H. Hu, D.D. Li, J. Chen, M.F. Luo, Unravelling the efficient catalytic performance of ozone decomposition over nitrogen-doped manganese oxide catalysts under high humidity, N. J. Chem. 44 (2020) 17993–17999, https://doi.org/10.1039/D0NJ04393A.

[19] T. Gopi, G. Swetha, S.C. Shekar, C. Ramakrishna, B. Saini, R. Krishna, P.V.L. Rao, Catalytic decomposition of ozone on nanostructured potassium and proton containing δ-MnO_2 catalysts, Catal. Commun. 92 (2017) 51–55, https://doi.org/10.1016/j.catcom.2017.01.002.

[20] G. Abdallah, R. Bitar, S.K.P. Veerapandian, J.M. Giraudon, N.D. Geyter, R. Morent, J.F. Lamonier, Acid treated Ce modified birnessite-type MnO_2 for ozone decomposition at low temperature: effect of nitrogen containing co-pollutants and water, Appl. Surf. Sci. 571 (2022) 151240, https://doi.org/10.1016/j.apsusc.2021.151240.

[21] W. Hong, M.P. Shao, T.L. Zhu, H.N. Wang, Y. Sun, F.X. Shen, X. Li, To promote ozone catalytic decomposition by fabricating manganese vacancies in ε-MnO_2 catalyst via selective dissolution of Mn-Li precursors, Appl. Catal. B 274 (2020) 119088, https://doi.org/10.1016/j.apcatb.2020.119088.

[22] G.X. Zhu, J.G. Zhu, W.J. Jiang, Z.J. Zhang, J. Wang, Y.F. Zhu, Surface oxygen vacancy induced α-MnO_2 nanofiber for highly efficient ozone elimination, Appl. Catal. B 209 (2017) 118963, https://doi.org/10.1016/j.apcatb.2017.02.068.

[23] X.T. Li, J.Z. Ma, L. Yang, G.Z. He, C.B. Zhang, R.D. Zhang, H. He, Oxygen vacancies induced by transition metal doping in γ-MnO_2 for highly efficient ozone decomposition, Environ. Sci. Technol. 52 (2018) 12685–12696, https://doi.org/10.1021/acs.est.8b04294.

[24] Y. Yu, S.L. Liu, J. Ji, H.B. Huang, Amorphous MnO_2 surviving calcination: an efficient catalyst for ozone decomposition, Catal. Sci. Technol. 9 (2019) 5090–5099, https://doi.org/10.1039/C9CY01426H.

[25] H. Yu, J.W. Yang, L.L. Lu, Y.C. Guo, J. Guan, G.J. Fan, Q.Y. Zhu, N. Han, Y.F. Chen, Controllable synthesis of different MnO_2 phases by a precipitation method for effective ozone decomposition, J. Phys. Chem. C (2024), https://doi.org/10.1021/acs.jpcc.4c00465.

[26] G.X. Zhu, W. Zhu, Y. Lou, J. Ma, W.Q. Yao, R.L. Zong, Y.F. Zhu, Encapsulate α-MnO_2 nanofiber within graphene layer to tune surface electronic structure for efficient ozone decomposition, Nat. Commun. 12 (2021) 4152, https://doi.org/10.1038/s41467-021-24424-x.

[27] X.T. Li, J.Z. Ma, H. He, Recent advances in catalytic decomposition of ozone, J. Environ. Sci. 94 (2020) 14–31, https://doi.org/10.1016/j.jes.2020.03.058.

[28] X. Chen, Z.L. Zhao, S. Liu, J.X. Huang, J. Xie, Y. Zhou, Z.Y. Pan, H.F. Lu, Ce-Fe-Mn ternary mixed-oxide catalysts for catalytic decomposition of ozone at ambient temperatures, J. Rare Earth 38 (2020) 175–181, https://doi.org/10.1016/j.jre.2019.01.010.

[29] C.L. Chen, J. Xie, X. Chen, W.X. Zhang, J. Chen, A.P. Jia, Cu Species-modified OMS-2 materials for enhancing ozone catalytic decomposition under humid conditions, ACS Omega 8 (2023) 19632–19644, https://doi.org/10.1021/acsomega.3c01186.

[30] L.G. Tao, G.F. Zhao, P.J. Chen, Z.Q. Zhang, Y. Liu, Y. Lu, High-performance Co-MnO_x composite oxide catalyst structured onto Al-fiber felt for high-throughput O_3 decomposition, ChemCatChem 11 (2019) 1131–1142, https://doi.org/10.1002/cctc.201801401.

[31] Y.J. Yang, D. Shen, P.Y. Zhang, The effect of heat treatment in different atmospheres on tungsten-doped MnO_2 for ozone decomposition, Ozone. Sci. Eng. 43 (2021) 195–206, https://doi.org/10.1080/01919512.2020.1772040.

[32] M. Chernykh, M. Grabchenko, A. Knyazev, G. Mamontov, Cordierite-supported transition-metal-oxide-based catalysts for ozone decomposition, Crystals 13 (2023) 1674, https://doi.org/10.3390/cryst13121674.

[33] H. Liang, Q. Zheng, K.B. Zhang, Y.L. Yang, R. He, Mesoporous CeO_x/MnO_x catalyst derived from Mn-BTC for ozone catalytic decomposition, Appl. Catal. A 653 (2023) 119080, https://doi.org/10.1016/j.apcata.2023.119080.

[34] R.R. Cao, L.X. Li, P.Y. Zhang, L.L. Gao, S.P. Rong, Regulating oxygen vacancies in ultrathin δ-MnO_2 nanosheets with superior activity for gaseous ozone decomposition, Environ. Sci. Nano 8 (2021) 1628–1641, https://doi.org/10.1039/D1EN00149C.

[35] G.X. Zhu, J.G. Zhu, W.L. Li, W.Q. Yao, R.L. Zong, Y.F. Zhu, Q.F. Zhang, Tuning the K+ concentration in the tunnels of α-MnO_2 to increase the content of oxygen vacancy for ozone elimination, Environ. Sci. Technol. 52 (2018) 8684–8692, https://doi.org/10.1021/acs.est.8b01594.

[36] W. Hong, T.L. Zhu, Y. Sun, H.N. Wang, X. Li, F.X. Shen, Enhancing oxygen vacancies by introducing Na^+ into OMS-2 tunnels to promote catalytic ozone decomposition, Environ. Sci. Technol. 53 (2019) 13332–13343, https://doi.org/10.1021/acs.est.9b03689.

[37] W.J. Dai, B.G. Zhang, J. Ji, B.Y. Liu, R.J. Xie, Y.L. Gan, X.W. Xie, J.R. Zhang, P. L. Huang, H.B. Huang, Exceptional ozone decomposition over δ-MnO_2/AC under an entire humidity environment, Environ. Sci. Technol. 57 (2023) 17727–17736, https://doi.org/10.1021/acs.est.3c00717.

[38] S.J. Liu, W.J. Dai, B.Y. Liu, S.X. Lin, F. Zeng, Q.X. Huang, M. Sun, F.D. Feng, B. Lan, H.B. Huang, Highly c-disordered birnessite with abundant out-of-layer oxygen vacancies for enhanced ozone catalytic decomposition, Sep. Purif. Technol. 322 (2023) 124254, https://doi.org/10.1016/j.seppur.2023.124254.

[39] A.J. Wang, Y. Wu, X.H. Shen, Q.Y. Zhang, H.W. Jian, C. Han, Efficient ozone decomposition by amorphous Mn–Ni bimetallic catalysts under an entire humidity environment, J. Environ. Chem. Eng. 12 (2024) 113848, https://doi.org/10.1016/j.jece.2024.113848.

[40] Y.H. Zhu, L.Y. Yang, J.M. Ma, Y.R. Fang, J. Yang, X.P. Chen, J. Zheng, S.H. Zhang, W. Chen, C.Q. Pan, B.J. Zhang, X.F. Qiu, Z. Luo, J.L. Wang, Y.B. Guo, Rapid ozone decomposition over water-activated monolithic MoO_3/graphdiyne nanowalls under high humidity, Angew. Chem. Int. Ed. 62 (2023) e202309158, https://doi.org/10.1002/anie.202309158.

[41] J.Z. Ma, Y.F. Chen, G.Z. He, H. He, A robust H-transfer redox mechanism determines the high-efficiency catalytic performance of layered double hydroxides, Appl. Catal. B 285 (2021) 119806, https://doi.org/10.1016/j.apcatb.2020.119806.

[42] H. Wang, P. Rassu, X. Wang, H.W. Li, X.R. Wang, X.Q. Wang, X. Feng, A.X. Yin, P. F. Li, X. Jin, S.L. Chen, X.J. Ma, B. Wang, An iron-containing metal-organic framework as a highly efficient catalyst for ozone decomposition, Angew. Chem. Int. Ed. 57 (2018) 16416–16420, https://doi.org/10.1002/anie.201810268.

[43] Z.B. Sun, Y.N. Si, S.N. Zhao, Q.Y. Wang, S.Q. Zang, Ozone decomposition by a manganese-organic framework over the entire humidity range, J. Am. Chem. Soc. 143 (2021) 5150–5157, https://doi.org/10.1021/jacs.1c01027.

[44] Y.J. Yang, D. Shen, P.Y. Zhang, The effect of heat treatment in different atmospheres on tungsten-doped MnO_2 for ozone decomposition, Ozone. Sci. Eng. 43 (2021) 195–206, https://doi.org/10.1080/01919512.2020.1772040.

[45] J.F. Deng, H.X. Li, W.J. Wang, Progress in design of new amorphous alloy catalysts, Catal. Today 51 (1999) 113–125, https://doi.org/10.1016/S0920-5861(99)00013-9.

[46] A. Lyer, J. Del-Pilar, C.K. King'ondu, E. Kissel, H.F. Garces, H. Huang, A.M. El-Sawy, P.K. Dutta, S.L. Suib, Water oxidation catalysis using amorphous manganese oxides, octahedral molecular sieves (OMS-2), and octahedral layered (OL-1) manganese oxide structures, J. Phys. Chem. C 116 (2012) 6474–6483, https://doi.org/10.1021/jp2120737.

[47] H.R. Tang, Z.H. Wang, J.M. Shao, F.W. Lin, P.X. Liu, Y. He, Y.Q. Zhu, Catalytic decomposition of residual ozone over cactus-like MnO_2 nanosphere: synergistic mechanism and SO_2/H_2O interference, ACS Omega 7 (2022) 9818–9833, https://doi.org/10.1021/acsomega.2c00120.

[48] B. Feng, J. Weng, B.C. Yang, S.X. Qu, X.D. Zhang, Characterization of surface oxide films on titanium and adhesion of osteoblast, Biomaterials 24 (2003) 4663–4670, https://doi.org/10.1016/S0142-9612(03)00366-1.

[49] G.Y. Chen, Z. Wang, F.W. Lin, Z.M. Zhang, H.D. Yu, B.B. Yan, Z.H. Wang, Comparative investigation on catalytic ozonation of VOCs in different types over supported MnO_x catalysts, J. Hazard. Mater. 391 (2020) 122218, https://doi.org/10.1016/j.jhazmat.2020.122218.
[50] J.H. He, T.J. Wang, X.Q. Bi, Y.B. Tian, C.D. Huang, W.B. Hu, Z. Wang, B. Jiang, Y. M. Gao, Y.Y. Zhu, X.D. Wang, Subsurface A-site vacancy activates lattice oxygen in perovskite ferrites for methane anaerobic oxidation to syngas, Nat. Commun. 15 (2024) 5422, https://doi.org/10.1038/s41467-024-49776-y.
[51] S.Y. Lu, L.Z. Sui, J.J. Liu, S.J. Zhu, A.M. Chen, M.X. Jin, B. Yang, Near-infrared photoluminescent polymer–carbon nanodots with two-photon fluorescence, Adv. Mater. 29 (2017) 1603443, https://doi.org/10.1002/adma.201603443.
[52] M. Schindler, F.C. Hawthorne, M.S. Freund, P.C. Burns, XPS spectra of uranyl minerals and synthetic uranyl compounds. II: the O 1s spectrum, Geochim. Cosmochim. Acta 73 (2009) 2488–2509, https://doi.org/10.1016/j.gca.2008.10.041.
[53] Z.S. Han, C. Choi, S. Hong, T.S. Wu, Y.L. Soo, Y.S. Jung, J.S. Qiu, Z.Y. Sun, Activated TiO_2 with tuned vacancy for efficient electrochemical nitrogen reduction, Appl. Catal. B 257 (2019) 117896, https://doi.org/10.1016/j.apcatb.2019.117896.
[54] V. Natu, M. Benchakar, C. Canaff, A. Habrioux, S. Célérier, M.W. Barsoum, A critical analysis of the X-ray photoelectron spectra of Ti_3C_2Tz MXenes, Matter 4 (2021) 1224–1251, https://doi.org/10.1016/j.matt.2021.01.015.
[55] Y.M. Fan, F. Wang, R.T. Li, C.H. Liu, Q. Fu, Surface hydroxyl-determined migration and anchoring of silver on alumina in oxidative redispersion, ACS Catal. 13 (2023) 2277–2285, https://doi.org/10.1021/acscatal.2c05453.
[56] L.T. Zhuravlev, The surface chemistry of amorphous silica. Zhuravlev model, Colloids Surf. A 173 (2000) 1–38, https://doi.org/10.1016/S0927-7757(00)00556-2.
[57] T. Cai, Z. Liu, J. Yuan, P. Xu, K.F. Zhao, Q. Tong, W.Q. Lu, D.N. He, The structural evolution of MnO_x with calcination temperature and their catalytic performance for propane total oxidation, Appl. Surf. Sci. 565 (2021) 150596, https://doi.org/10.1016/j.apsusc.2021.150596.
[58] T. Bezrodna, G. Puchkovska, V. Shymanovska, J. Baran, H. Ratajczak, IR-analysis of H-bonded H_2O on the pure TiO_2 surface, J. Mol. Struct. 700 (2004) 175–181, https://doi.org/10.1016/j.molstruc.2003.12.057.
[59] S. Kudo, S. Nakashima, Changes in IR band areas and band shifts during water adsorption to lecithin and ceramide, Spectrochim. Acta Part A 228 (2020) 117779, https://doi.org/10.1016/j.saa.2019.117779.
[60] H. Noei, H.S. Qiu, Y.M. Wang, E. Löffler, C. Wöll, M. Muhler, The identification of hydroxyl groups on ZnO nanoparticles by infrared spectroscopy, Phys. Chem. Chem. Phys. 10 (2008) 7092–7097, https://doi.org/10.1039/B811029H.
[61] H. Yamagishi, S. Nakashima, Y. Ito, High temperature infrared spectra of hydrous microcrystalline quartz, Phys. Chem. Miner. 24 (1997) 66–74, https://doi.org/10.1007/s002690050018.
[62] M. Richter, A. Trunschke, U. Bentrup, K.W. Brzezinka, E. Schreier, M. Schneider, M.M. Pohl, R. Fricke, Selective catalytic reduction of nitric oxide by ammonia over egg-shell MnO_x/NaY composite catalysts, J. Catal. 206 (2002) 98–113, https://doi.org/10.1006/jcat.2001.3468.
[63] Y.H. Li, B.G. Zhao, Y.M. Ma, P.Y. Liang, T.J. Sun, Synthetic effect of supports in Cu-Mn-doped oxide catalysts for promoting ozone decomposition under humid environment, Environ. Sci. Pollut. Res. 30 (2023) 102880–102893, https://doi.org/10.1007/s11356-023-29642-y.
[64] A. Khan, X.J. Feng, C.K. Yin, H. Ullah, A.A. Tahir, B.W. Li, W.M. Wang, X.X. Li, A. H. Xu, Mn_2O_3@Mn_5O_8 as an efficient catalyst for the degradation of organic contaminants in aqueous media through sulfite activation, Sep. Purif. Technol. 299 (2022) 121717, https://doi.org/10.1016/j.seppur.2022.121717.
[65] B.B. Chen, B. Wu, L.M. Yu, M. Crocker, C. Shi, Investigation into the catalytic roles of various oxygen species over different crystal phases of MnO_2 for C_6H_6 and HCHO oxidation, ACS Catal. 10 (2020) 6176–6187, https://doi.org/10.1021/acscatal.0c00459.
[66] A.S. Poyraz, J.P. Huang, C.J. Pelliccione, X. Tong, S.B. Cheng, L.J. Wu, Y.M. Zhu, A. C. Marschilok, K.J. Takeuchi, E.S. Takeuchi, Synthesis of cryptomelane type α-MnO_2 ($K_xMn_8O_{16}$) cathode materials with tunable K^+ content: the role of tunnel cation concentration on electrochemistry, J. Mater. Chem. A 5 (2017) 16914–16928, https://doi.org/10.1039/C7TA03476H.
[67] M. Chigane, M. Ishikawa, Manganese oxide thin film preparation by potentiostatic electrolyses and electrochromism, J. Electrochem. Soc. 147 (2000) 2246, https://doi.org/10.1149/1.1393515.
[68] A.S. Poyraz, J.P. Huang, L.J. Wu, D.C. Bock, Y.M. Zhu, A.C. Marschilok, K. J. Takeuchi, E.S. Takeuchi, Potassium-based α-manganese dioxide nanofiber binder-free self-supporting electrodes: a design strategy for high energy density batteries, Energy Technol. 4 (2016) 1358–1368, https://doi.org/10.1002/ente.201600128.
[69] Y.S. Pan, X.S. Zheng, G.Q. Zhao, Z.P. Rao, W.C. Yu, B.L. Chen, C.H. Chu, Water vapor condensation on iron minerals spontaneously produces hydroxyl radical, Environ. Sci. Technol. 57 (2023) 8610–8616, https://doi.org/10.1021/acs.est.3c01379.
[70] H.X. Hao, I. Leven, T. Head-Gordon, Can electric fields drive chemistry for an aqueous microdroplet? Nat. Commun. 13 (2022) 280, https://doi.org/10.1038/s41467-021-27941-x.
[71] H.Q. Xiong, J.K. Lee, R.N. Zare, W. Min, Strong electric field observed at the interface of aqueous microdroplets, J. Phys. Chem. Lett. 11 (2020) 7423–7428, https://doi.org/10.1021/acs.jpclett.0c02061.
[72] C.J. Wu, S.L. Cheng, Y.J. Sheng, H.K. Tsao, Reduction-assisted sintering of micron-sized copper powders at low temperature by ethanol vapor, RSC Adv. 5 (2015) 53275–53279, https://doi.org/10.1039/C5RA08167J.
[73] L.C. Yang, Q.S. Gao, Y. Tang, Y.P. Wu, R. Holze, MoO_2 synthesized by reduction of MoO_3 with ethanol vapor as an anode material with good rate capability for the lithium ion battery, J. Power Sources 179 (2008) 357–360, https://doi.org/10.1016/j.jpowsour.2007.12.099.
[74] Z.S. Wang, Y.F. Chen, X.T. Li, J.Z. Ma, G.Z. He, H. He, A superior catalyst for ozone decomposition: NiFe layered double hydroxide, J. Environ. Sci. 134 (2023) 2–10, https://doi.org/10.1016/j.jes.2021.12.016.